ARMY RESEARCH LABORATORY

Spatial Mechanical Response and Strain Gradient Evolution of Friction Stir Welded Aluminum-2139

by Brian Justusson, Jessica Medintz, Jian Yu, Constantine Fountzoulas, and Chian-Fong Yen

ARL-TR-5892 **February 2012**

NOTICES

Disclaimers

The findings in this report are not to be construed as an official Department of the Army position unless so designated by other authorized documents.

Citation of manufacturer's or trade names does not constitute an official endorsement or approval of the use thereof.

Destroy this report when it is no longer needed. Do not return it to the originator.

Army Research Laboratory
Aberdeen Proving Ground, MD 21005-5069

ARL-TR-5892 **February 2012**

Spatial Mechanical Response and Strain Gradient Evolution of Friction Stir Welded Aluminum-2139

Brian Justusson and Jessica Medintz
Oak Ridge Institute for Science and Education

Jian Yu, Constantine Fountzoulas, and Chian-Fong Yen
Weapons and Materials Research Directorate, ARL

REPORT DOCUMENTATION PAGE	Form Approved OMB No. 0704-0188

1. REPORT DATE *(DD-MM-YYYY)*	2. REPORT TYPE	3. DATES COVERED (From - To)
February 2012	Final	July 2007–August 2011

4. TITLE AND SUBTITLE
Spatial Mechanical Response and Strain Gradient Evolution of Friction Stir Welded Aluminum-2139

5a. CONTRACT NUMBER
ORISE 1120-1120-99

5b. GRANT NUMBER

5c. PROGRAM ELEMENT NUMBER

6. AUTHOR(S)
Brian Justusson,* Jessica Medintz,* Jian Yu, Constantine Fountzoulas, and Chian-Fong Yen

5d. PROJECT NUMBER
H84

5e. TASK NUMBER

5f. WORK UNIT NUMBER

7. PERFORMING ORGANIZATION NAME(S) AND ADDRESS(ES)
U.S. Army Research Laboratory
ATTN: RDRL-WMM-B
Aberdeen Proving Ground, MD 21005-5069

8. PERFORMING ORGANIZATION REPORT NUMBER
ARL-TR-5892

9. SPONSORING/MONITORING AGENCY NAME(S) AND ADDRESS(ES)
Oak Ridge Institute for Science and Education
MC-100-44, P.O. Box 117
Oak Ridge, TN 37831-0117

10. SPONSOR/MONITOR'S ACRONYM(S)
ORISE

11. SPONSOR/MONITOR'S REPORT NUMBER(S)

12. DISTRIBUTION/AVAILABILITY STATEMENT
Approved for public release; distribution is unlimited.

13. SUPPLEMENTARY NOTES
*Oak Ridge Institute for Science and Education, Oak Ridge, TN 37831

14. ABSTRACT
With current involvements of the U.S. Military in various peace-keeping and combat operations throughout the world, there is an increase in the deployment of armored military vehicles. Traditional armoring techniques have performed well against particular threats, but, in the recent combat operations, a new threat of improvised explosive devices, the vulnerability of the undercarriage, is being exposed. While thick, steel-structural members have been used in the past, an effort to make them more agile and deployable has caused a push toward lightweight materials. Advanced aluminum alloys, such as AA-2139, are attractive candidates because of their high strength and lower density than steel. Single-body construction can eliminate joint failure but requires a new joining technique. Friction stir welding (FSW) is a solid-state joining technique that combines extreme plastic deformation coupled with localized heat flux to create unique microstructure joints. In general, the mechanical properties are dependent on the formation of the microstructure. To the best of our knowledge, these microstructural zones and the quality of the weld have not fully been characterized under blast loading. Finite-element simulations have been used to predict the mechanical response of blast loading, but the effects of the microstructural zones on blast loading are not fully understood. In the present work, the spatial mechanical response of a FSW joint is analyzed to determine the spatial mechanical properties.

15. SUBJECT TERMS
microstructural evaluation, mechanical properties friction-stir, joints, SEM

16. SECURITY CLASSIFICATION OF:			17. LIMITATION OF ABSTRACT	18. NUMBER OF PAGES	19a. NAME OF RESPONSIBLE PERSON
a. REPORT	b. ABSTRACT	c. THIS PAGE			Brian Justusson
Unclassified	Unclassified	Unclassified	UU	30	19b. TELEPHONE NUMBER (*Include area code*) 410-306-0844

Contents

List of Figures

List of Tables

INTENTIONALLY LEFT BLANK.

1. Introduction/Background

Aluminum alloys are becoming increasingly desirable structural metals for replacing steel due to their lower density, 2.67 and 7.87 g/cm^3, respectively, and excellent specific bending stiffness. To date, armored vehicles rely heavily on steel armor, which increases the vehicles' own weight. There is a need for new lightweight personal and vehicular armor protection, which involves replacing steel with light metals. The creation of an aluminum chassis for armored vehicles can greatly reduce the weight of the vehicle; however, an optimized joining process is needed. Friction stir welding (FSW) is a solid-state joining technique developed in 1991 (*1*,*2*), and it is currently used extensively to weld commercial-grade advanced aluminum alloys. FSW is an optimal process for welding aluminum, in comparison to conventional welding techniques that are difficult to fuse together due to the aluminum oxide (Al_2O_3) formed on the surface (*3*). FSW reduces the cracks and voids that are formed during other joining processes.

FSW involves the use of a welding tool which consists of concentric cylinders composed of a thinner cylinder, known as a probe or pin, and a wider cylinder known as a shoulder (see figure 1). The probe or pin is pushed into the material after a critical softening temperature is reached and the flow stress is easily overcome due to local softening as a result of the heat flux. Once the tool is sunk into the material, it can be pulled past the stationary tool. As the material is pulled past the tool, distinct and unique microstructures develop as a function of the distance from the center of welding. These microstructures are generally referred to as the heat-affected zone (HAZ), which is a result of the heat dissipating through the material that promotes grain growth and dislocation annihilation, and the thermo-mechanically affected zone (TMAZ), which is a result of competing mechanisms due to the local heat flux promoting grain growth and dislocation annihilation and localized severe plastic deformation which results in decreased grain size. In particular, a microstructure, which is located near the center of the weld and termed the weld-nugget, is a fine, equiaxed grain structure. These zones have been shown to display unique mechanical properties (*3*). While the ductility of the alloy in the zone remains largely constant, the yield strength and ultimate tensile strength can be reduced. Studies have shown that the microstructures are a result of dynamic recrystallization and are very dependent on the stir parameters. Hirata et al. (*4*) showed that grain size decreases with weld velocity and increases with rotational speed.

Previous studies of friction stir welds of aluminum alloys show these unique microstructures exist and vary throughout the joint. Sutton et al. (*5*) have shown structures are extremely dependent on heat dissipation as grain growth rates vary through thickness in joints as small as 7 mm. Also, Sullivan and Robson (*6*) have shown this is more prevalent and can vary by as much as 50% from the top of the weld to the bottom of the weld in a 20-mm-deep joint. Sullivan's weld, however, did not go through the thickness. Given that the U.S. Military might

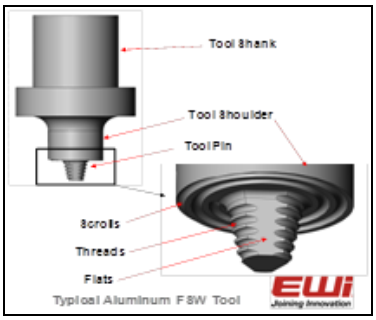

Figure 1. FSW tool.

require large joints for armoring purposes, a better understanding of the through-thickness properties needs to be better understood. To date, research efforts have failed to examine the effects of through-thickness weld joints in thick materials (≥20 mm) and the mechanical properties of the relatively new aluminum alloy 2139.

The objective of this effort is to investigate the macroscopic effects of the newly formed microstructural zones on the mechanical behavior of the FSW joint, specifically, the effect on the modulus of elasticity, failure strain, and ultimate tensile strength (UTS). These properties were derived from the experimental stress-strain curves of the alloy. In addition, the fracture surfaces of the failed specimens were observed under a scanning electron microscope (SEM), and the results of SEM fractography were used to understand the stress strain behavior. The current work will report the following:

1. The spatial stress-strain response and mechanical property models.
2. Analysis of fracture mode in the specimens.
3. Analysis of the strain-gradient hardening during testing.

2. Experiment/Calculations

2.1 Material

Two plates of AA-2139, high-strength, high-damage tolerant, quaternary aluminum-magnesium-silver-copper solid solution alloy (*7*) were welded together as an FSW joint using the parameters shown in table 1, which had been shown to be optimal parameters in past welds. The solubility limits of AA-2139 are given in table 2. The plates were welded at the Edison Welding Institute (EWI) in Dayton, OH. The FSW tool was a two-piece tool with four flats and a left-handed thread, similar to the one shown in figure 1.

Table 1. FSW parameters.

Parameter	Specification
Shoulder diameter	1.625 in
Pin length	0.972 in
Plunge depth	0.65–0.005 in
Spindle speed	150–250 rpm
Travel speed	2 in/min
Total length	18 in

Table 2. Solubility limits of AA-2139.

	Si	Fe	Cu	Mn	Mg	Cr	Zn	Ti	Ag	V
Limits	0.1	0.15	4.5–5.5	0.2–0.6	0.2–0.8	0.05	0.25	0.15	0.15–0.6	0.05

Global tensile and bending tests were performed at EWI for the weld and were determined to be within specification for weld quality. Dog-bone samples were cut from the welded AA-2139 plates (figure 2). The specimens were marked according to the group on the alloy they were cut from, and its location in the plate.

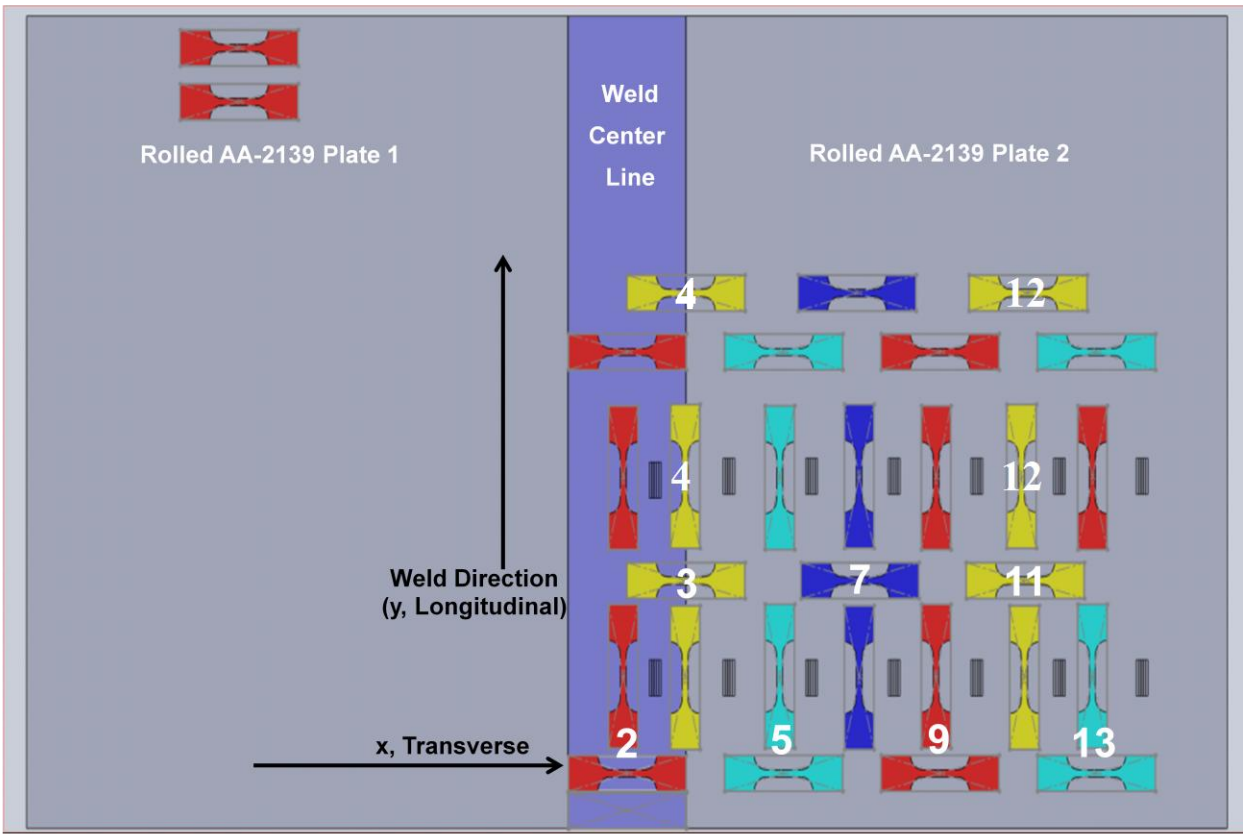

Figure 2. Dog-bone samples location.

2.2 Tensile Testing Method

Tensile testing was performed on a screw-driven Instron 1125. Dog-bone samples from the plate discussed in section 2.1 were cut using electric-discharge machining at various places in the weldment shown in figure 3. Prior to testing, the thickness and width of the samples were measured three times and the statistical average was used to determine the cross sectional area of each sample.

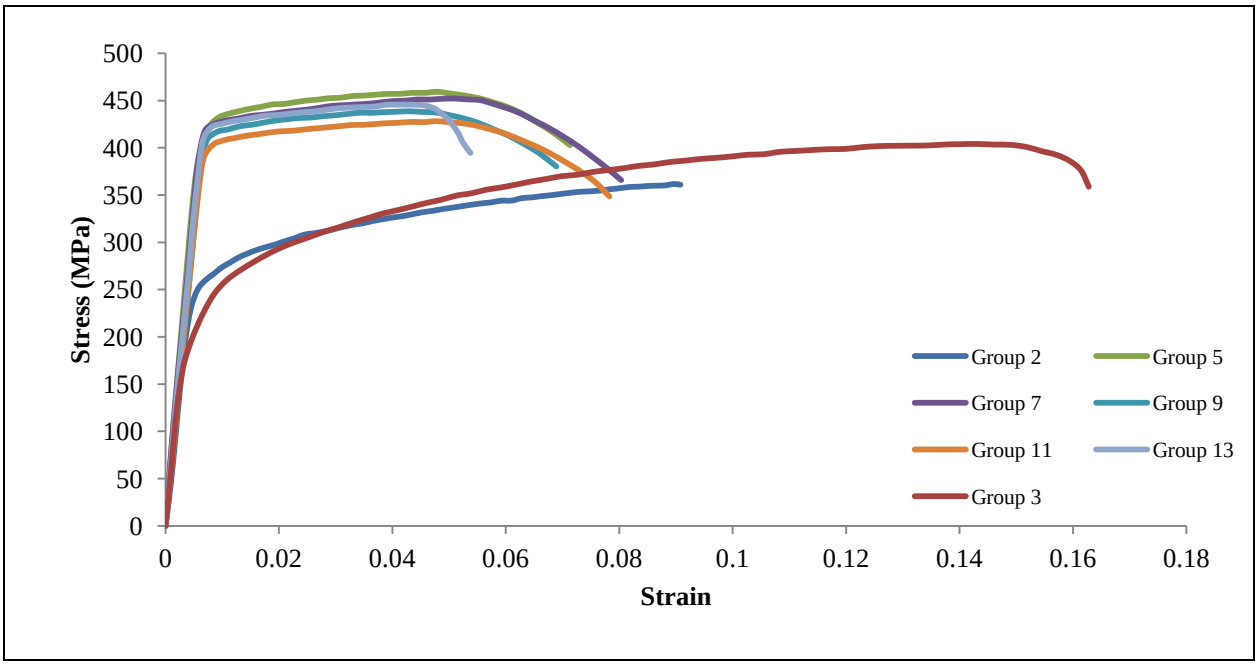

Figure 3. Tensile results in X direction.

The test was displacement controlled at a rate of 0.004 in/min (0.1 mm/min) to create a quasi-static loading condition. A 1000-lb load cell was used. Load (N), displacement (mm), and time (s) were all measured by the Instron during testing. Photos were taken every 15 s using a Nikon D300 with a 70-mm lens attached fitted with a lens extender. The shutter speed was set to 6 s. The photos taken were analyzed in commercially available digital image correlation software (Aramis V6.2), and the images were correlated to the data collected by using the time history from Instron data. The strain was calculated internal to the program using the ratio of the change in length to length from each picture compared to the first image and the results plotted as stress versus strain. From this graph, the modulus of elasticity, UTS, and the percent-failure strain were calculated.

After data reduction, it was determined that additional samples should be cut for testing to understand the through-thickness effects in the welded area relative to the unaffected area. The remaining tensile samples from group 2, in both the x and y direction, were cut to nominal thicknesses of 0.04 in (1 mm). Additionally, samples from groups 4 and 8 were cut in the same

fashion. The tensile-testing procedure remained the same; however, shutter speed was adjusted to 1 s, and photos were taken in 5-s intervals.

2.3 Fractography

The surfaces of the fractured samples were examined by using an SEM (model Hitachi S-4700). To eliminate static electricity effects during SEM examination, a carbon conducting tape was attached to the specimen. The fractured surfaces of the specimen were examined at various magnifications, and general fracture behavior was observed.

2.4 Grinding/Polishing Method

Polishing was completed using a Stuer RotoPol-31 fitted with a Struer Rotoforce 4 automatic polisher head, using the steps shown in table 2. The grinding steps involved sand paper with the given grit size.

The polishing steps for 6 and 3 µm were performed on trident polishing cloths with water-based, diamond-suspension solutions. The final step for 0.05 µm was performed using colloidal silica. Between steps, the specimens were examined for scratches and cleaned using ethanol. A sodium hydroxide (NaOH) etchant was used for an application time of 1.5 min.

3. Results and Discussion

3.1 Tensile Results

The calculated directional mechanical properties of the AA-2139 groups are shown in table 3. Group 2 is the area in the weld, as shown in figure 3. Group 3 is the area that traverses the weld and the non-affected area. Groups 5–13 are all groups that have been cut from the non-affected area of the sample (figure 2). As shown in table 4, the modulus of elasticity is approximately 20% lower for groups 2 and 3 than the other groups. Additionally, a general trend was noticed: the modulus in the through-thickness (Z) direction was the lowest in all the samples. This is a result of the texturing in the grains that develops during cold working of the plates prior to welding and the severe plastic deformation during the FSW process. Similar results were reported in works by Yuana et al. (*8*) and Suhuddin et al. (*9*).

Table 3. Polishing procedure.

Step Type (Grit)	Time (min:s)
Grinding (120 paper)	Until flat
Grinding (320 paper)	1:30
Grinding (600 paper)	6:00
Grinding (1200 paper)	8:30
Polishing (6 µm)	10:00
Polishing (3 µm)	15:00
Polishing (0.05 µm)	2:00

Table 4. Mechanical properties of AA-2139.

Group No.	Direction	Sample No.	Modulus of Elasticity (GPa)	Ultimate Tensile Strength (MPa)	Failure Strain (%)	Fracture Characteristics
2	X	3	53.9	362	9.08	45°
—	Y	3	53.8	389	13.7	45°
—	Z	3	46.5	353	15.2	45°
3	X	2	56.7	404	16.3	45°
—	Z	2	51.7	384	10	45°
5	X	2	71.7	459	7.13	Moderately brittle ductile
—	Y	2	66.7	454	5.1	Moderately ductile
—	Z	2	50.6	424	7.3	Moderately ductile
7	X	2	68.9	452	8.04	Moderately ductile
—	Y	2	65.9	456	7.07	Moderately ductile
—	Z	2	54.5	416	7.45	Moderately ductile
9	X	2	61.7	439	6.89	Moderately brittle ductile
—	Y	2	60.8	444	7.21	Moderately ductile
—	Z	2	54	417	7.15	Moderately ductile
11	X	2	61.6	428	7.83	Moderately ductile
—	Y	2	67.7	440	3.21	Moderately ductile
—	Z	2	57.7	416	5.93	Moderately ductile
13	X	2	66.1	446	5.38	Moderately ductile
—	Y	2	66.7	439	4.32	Moderately ductile
—	Z	2	56.5	417	6.03	Moderately ductile

The stress-strain curves from the mechanical testing showed an interesting behavior, as seen in figures 3–5. Figure 3 shows the tensile results in X or transverse direction, whereas figure 4 shows the Y, or longitudinal (weld), direction, and figure 5 shows the through-thickness results. Of particular interest, groups 2 and 3 show the highest failure strain, but lowest UTS.

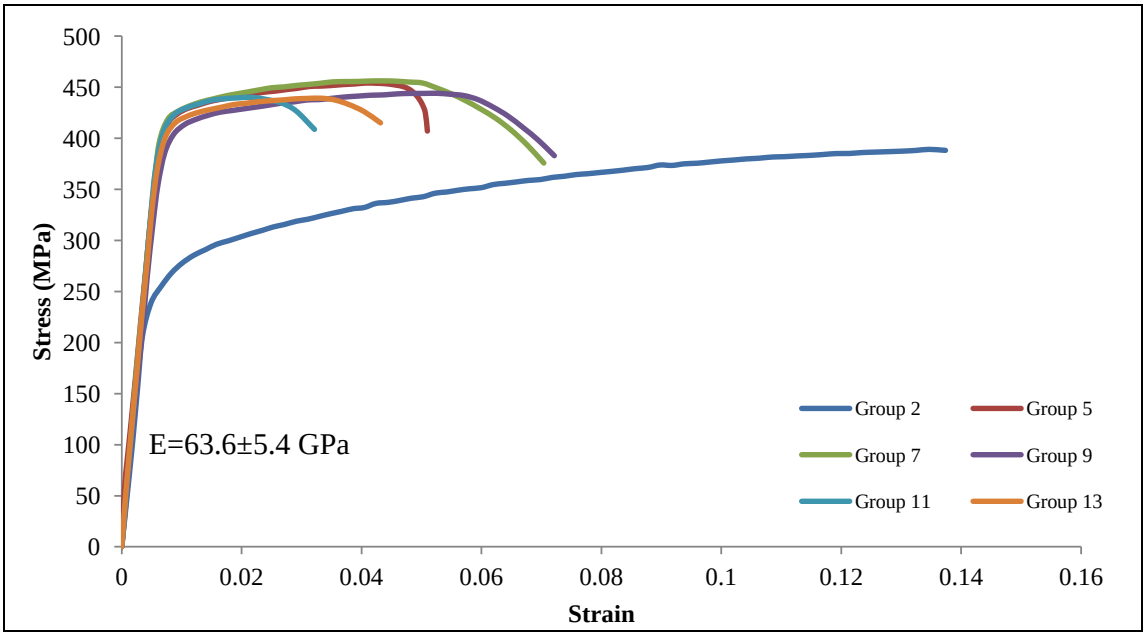

Figure 4. Tensile results in the Y direction.

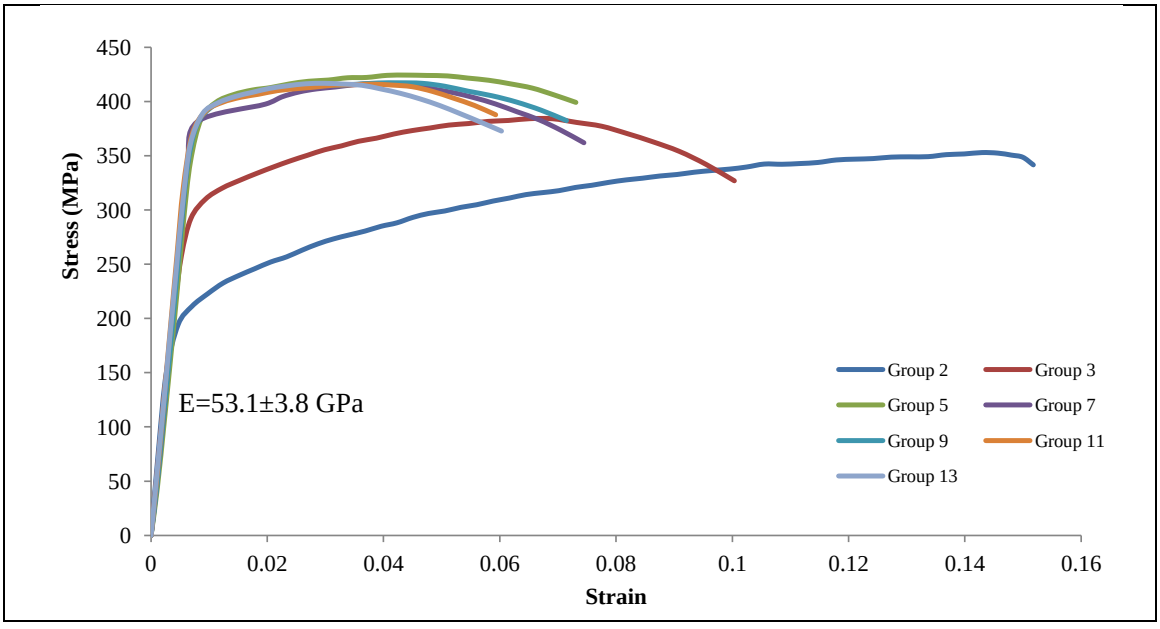

Figure 5. Tensile results in Z direction.

Conversely, groups 5 and higher showed remarkable similarities in behavior in failure strain, as well as ultimate tensile strength and failure strain in all directions. This would indicate that there are only spatial considerations for mechanical properties in the direct area of the weld.

From these results, it was determined the spatial considerations for mechanical properties are only important in the area of the weld; however, the through-thickness effects were not completely understood. These effects needed to be understood because microstructure varies in all directions around the weld and is most likely not constant through the thickness. In order to understand this effect, the through-thickness properties for groups 2, 4, and 12 were examined in greater detail; their profiles are shown in figures 6–8, which examine the effects of the through-thickness properties of the modulus of elasticity, the ultimate tensile strength, and failure strain, respectively.

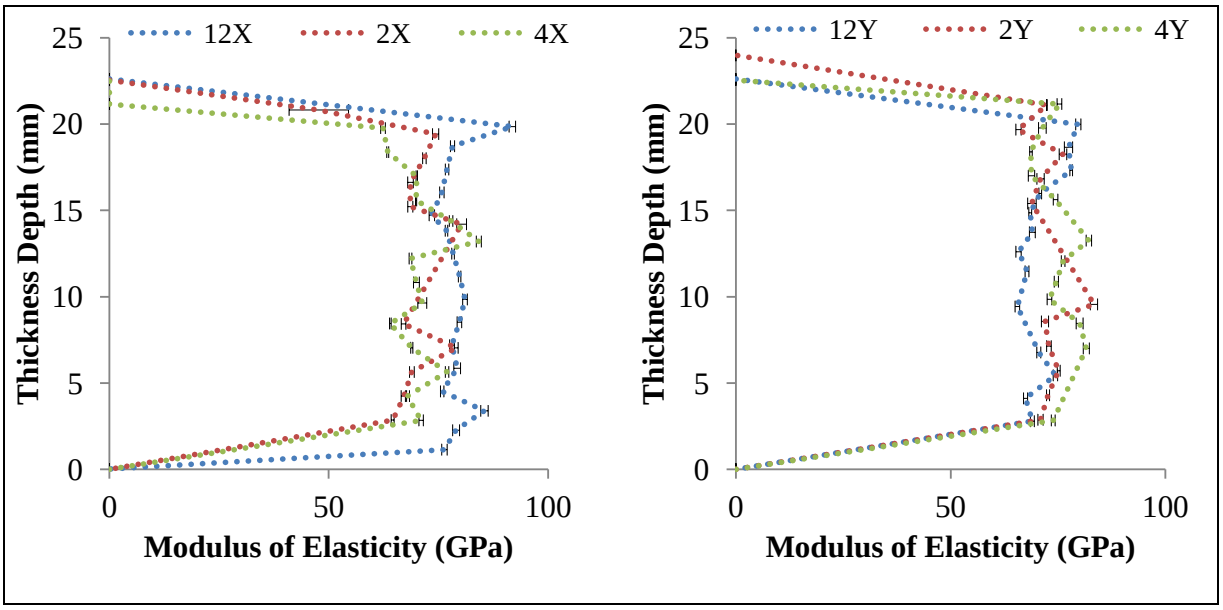

Figure 6. Modulus through-thickness distribution in X and Y directions for groups in the weld (2), along the weld (4), and unaffected (12).

From the results shown in figure 6, the modulus of elasticity in the X direction varied through the thickness with various degrees of deviation. As presented, figure 6 shows the through thickness where 0 corresponds to the bottom of the plate. In particular, the 12X (unaffected zone) sample displayed the least amount of deviation through the thickness, most likely as a result of the constant microstructure being far away from the heat generated during the friction-stir zone. The 4X (traverses weld) and 2X (on weld) groups showed the larger amounts of variation. In the Y direction, groups 2, 4, and 12 showed a similar amount of variation through the thickness

Figure 7 shows the results of the through-thickness tests for the UTS. Once again, the 12X and 12Y groups showed a general agreement as the samples are within the experimental error. The 2X and 2Y groups show a bimodal agreement with a gradient occurring through the thickness.

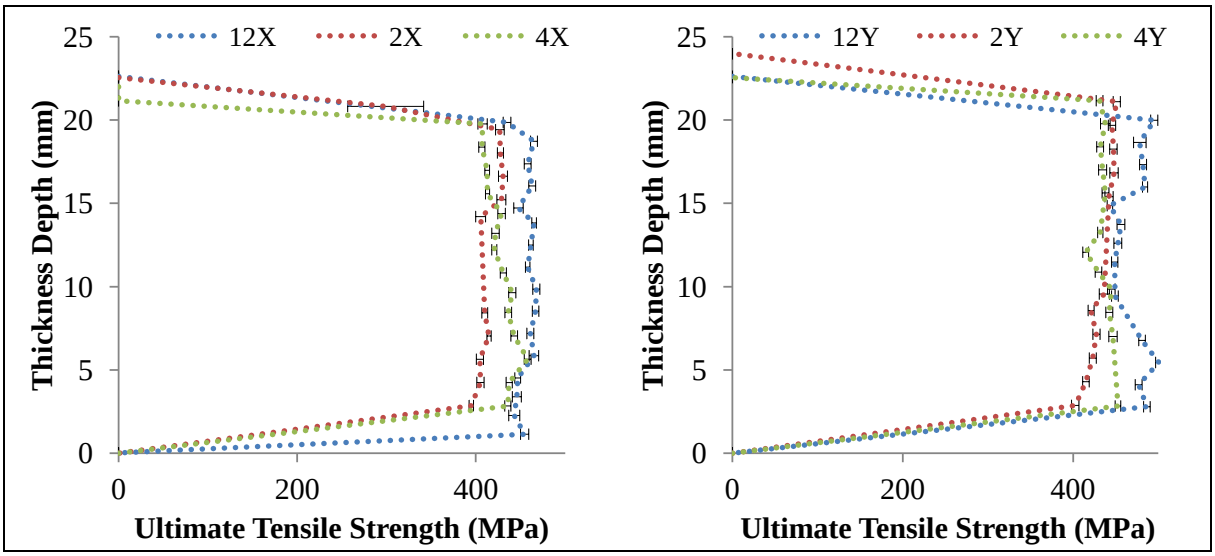

Figure 7. UTS through-thickness distribution in X and Y directions for groups in the weld (2), along the weld (4) and unaffected (12).

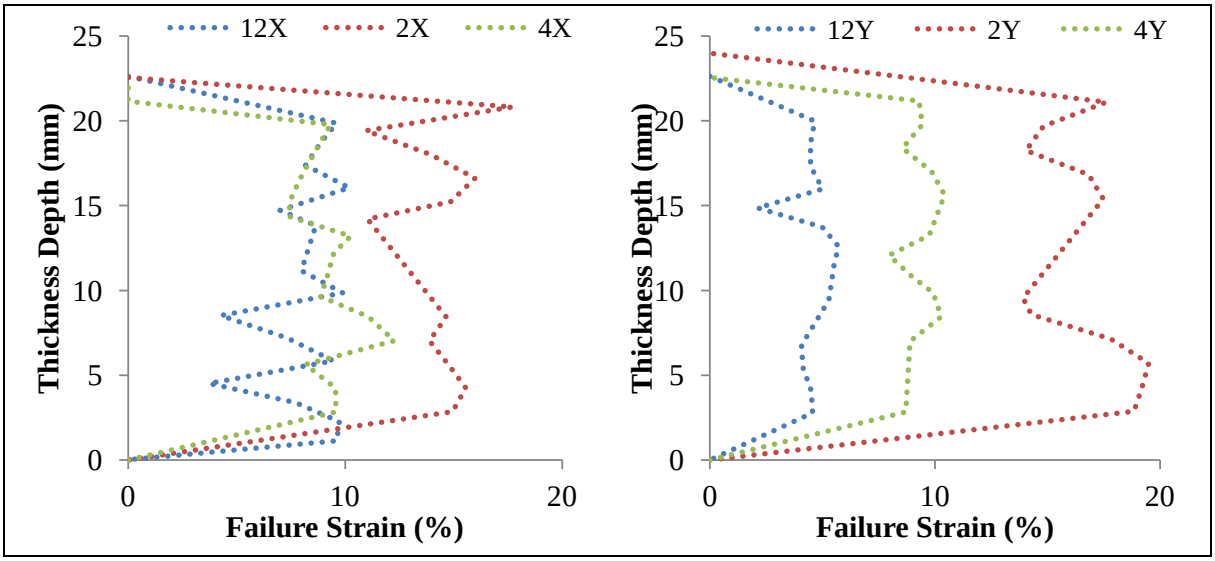

Figure 8. Failure strain through thickness distribution in X and Y directions for groups in the weld (2), along the weld (4), and unaffected (12)

This can be accounted for by the existence of a lower weld nugget in the bottom of the sample which has finer grains than that of the upper weld nugget. The coarser grains have higher work-hardening ability because they can support a higher saturation dislocation density and therefore, have a higher UTS. This accounts for the deviation through the thickness. This same higher-saturation dislocation density can explain the trend of the UTS being larger near the bottom of the weld for the 4X and 4Y samples. This is because the geometry of the tool allows for an angled interface with respect to the through-thickness direction. Because of how the samples are cut, at the top of the weld, the gauge section includes more of the weld nugget and less of the

coarser grained structures of the TMAZ and HAZ. Conversely, when cutting closer to the bottom, the coarser grained structures of the TMAZ and HAZ have a higher density in the gauge section. The coarser grained structures allow for higher work-hardening ability and, thus, higher UTS.

Figure 8 shows that the highest failure strain was in the group 2 samples in both the X and Y directions, the sample inside the weld. This sample also showed a very large amount of variation, but, in general, higher failure strains were observed at the top of the weld relative to the bottom. This is, once again, a microstructurally induced effect. The samples in groups 4 and 12 showed less variation, but, in general, the 4X had higher failure strains. This effect is much more apparent in the Y direction.

Figure 9 shows the comparison between the average through-thickness properties for the modulus of elasticity, UTS, and failure strain for both the X and Y directions as well as the difference between groups 2, 4, and 12. With respect to the modulus of elasticity, in the area of the weld, groups 2 and 4, the Y direction was on average higher; however, they are in agreement within experimental error. In the 12 group, the X direction showed an higher average modulus which is most likely an effect of the preprocess rolling of the AA-2139 plates.

The UTS shows, on average, the Y direction is higher; however, they are statistically insignificant due to agreement within experimental error. The conclusion that can be drawn is that UTS is microstructurally dependent, i.e., dependent on the lowest work- hardenable microstructure. This is because there is very little deviation in the UTS for the given groups and is in agreement within experimental error. The slight deviation demonstrates that the microstructural zones determine the UTS. This effect will be discussed more in the strain gradient hardening.

Finally, in the area around the welded zone, the Y direction was on average higher than the X direction. This is because of the distribution of grains throughout the welded region. Group Y samples in the 2 and 4 direction have a higher concentration of grains from the weld nugget. Since the weld nugget grains are generally fine and soft due to the results of dynamic recrystallization, they can go through high amounts of strain hardening due to rapid dislocation nucleation. For group 12, the UTS was lower for the Y direction which might be a result of more cold working in the Y direction prior to welding of the plates.

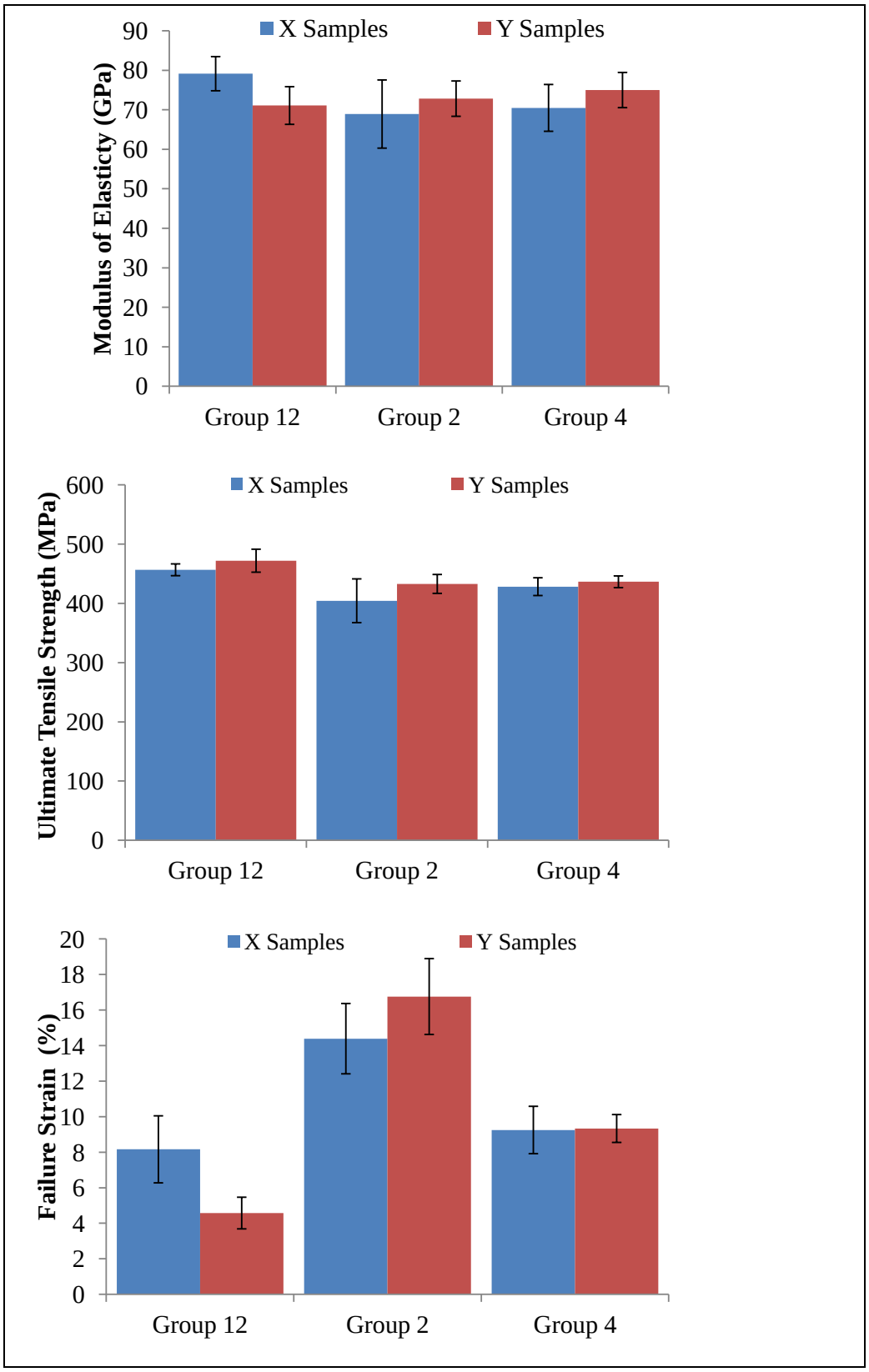

Figure 9. Comparison of through-thickness average for modulus of elasticity, UTS, and failure strain.

3.2 Fractography

In general, the material failure was ductile. On a macroscopic level, there were two types of characteristic failure patterns as shown in figures 10–13; these types are the commonly called cup and cone and material shear. Both types of failures are common in ductile failure. Cup and cone involves shear components of the stress state acting on opposite ends to form a chevron type of pattern, or cone. This failure is characterized by highly tensile failure in the end of the chevron, with shearing components on the side. The other failure mode common for ductile failure is the material shearing. This involves a single failure path that is characterized by a characteristic angle of nominally oriented at 45° to the samples free edge. Both types of failures were observed during testing and are indicated in table 4. The 45° failure corresponds to the shearing failure whereas moderately ductile would refer to the fracture surface containing cup and cone characteristics. The moderately brittle, ductile refers to zones that show high amounts of both shearing and tensile failure.

Fractography was used to observe the different causes of failure during testing. As shown in figures 3–5, the material behaved in a ductile manner as characterized by high-failure strains and noticeable work hardening. Comparing those graphs to the fractographic pictures taken, shown in figures 10–13, ductile failures can be observed. Typical ductile failure surfaces show two types of failure, tensile failure and shearing failure. Tensile failure is characterized by dimpling, which is a result high local plastic deformation. As a material strains, microvoids coalesce and form networks of fibrous dimples. Shear banding is the strip-like striations found in ductile materials (*10*). Shear bands form as a result of void link-up, which forms as a result of the shearing components in internal stress state. Figure 8 indicates that the failure of specimens in group 2 (the group inside the weld) is mostly pure tensile, failure, as shown by the large ratio of dimpling relative to the slight shear banding (right side of figure 8), Lee has also observed similar results for advanced aluminum FSW alloys (*11*). Figure 8 shows ductile failure patterns, characterized by very rough and irregular dimpling and shear banding.

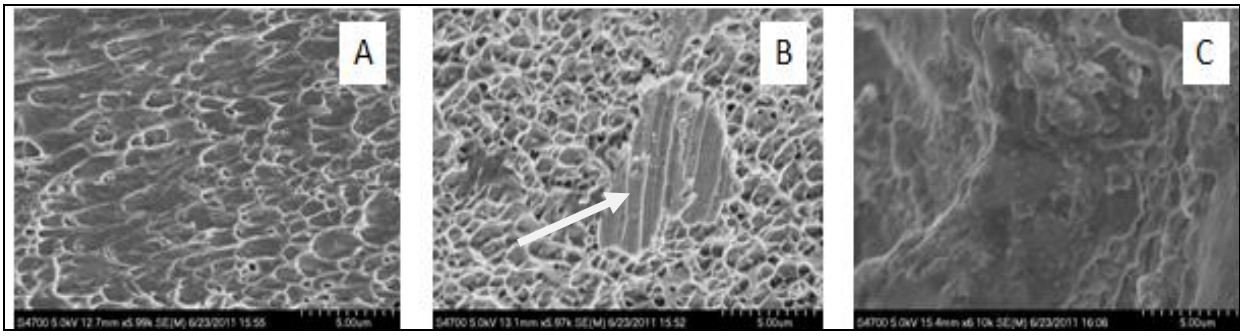

Figure 10. Group 2 failure patterns.

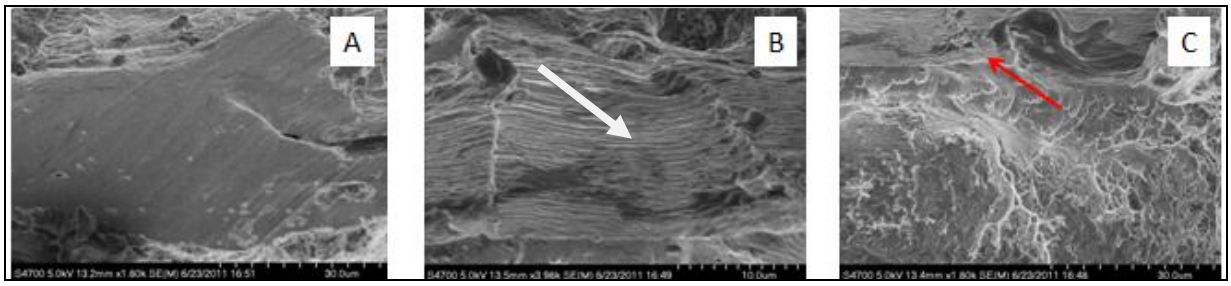

Figure 11. Group 3X failure patterns.

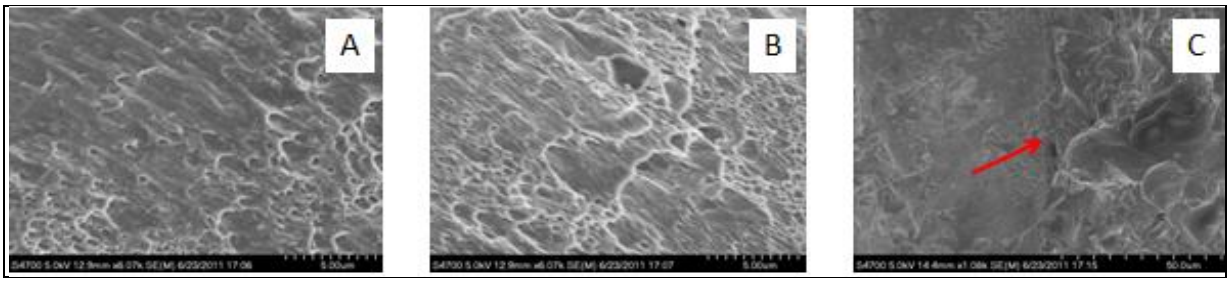

Figure 12. Group 3Y failure patterns.

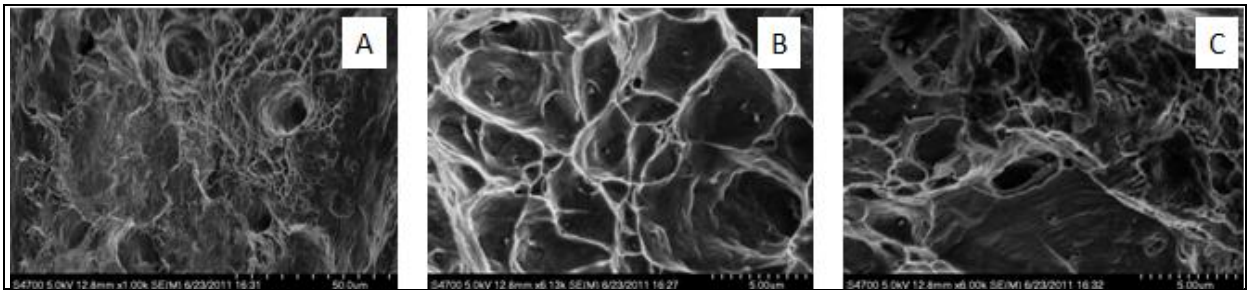

Figure 13. Group 13 failure patterns.

As shown in figure 11, the samples from group 3 (the samples that traversed the weld zone) show there is much more shear banding, as seen in figure 11B. This is a result of the stress state that developed during loading. Figure 11A shows a very large area of shearing; however, undercloser magnification in figure 11B, it is evident that heavy shear banding took place. Additionally, figure 11C shows a small amount of dimpling occurring, which is a result of the tensile component of the stress state.

The micrographs of group 3 in the Y direction, figure 12, show much more dimpling than that of the group 3 X direction. The shear banding is observed in fewer areas relative to that of group 3X in figure 11. Figures 12A and B show a very large amount of dimpling; this is characteristic of the tensile failure. Group 3 in the Y direction contained a large number of dimpling zones.

Figures 12A and B show elongated dimples which occurs from tear loading; they are signs of a ductile failure. Another interesting finding from these photomicrographs is the apparent separation from the non-affected area and the weld (figure 12C). When analyzing the failure

pattern, the specimen fails near the grip and not in the center of the gauge section. This may be a result of the various grain structures that form during FSW processing. In particular, this may be the separation between the various heat affected zones and the unaffected zones, or, in other words, this is the area in which heat dissipation in minimized or nonexistent. This can cause a large mismatch in material properties, which leads to a localized strain gradient due to the material not straining in a uniform manner. This effect will be discussed later in more detail.

Figure 13 shows the failure mode of group 13, the non-affected area. These specimens have a very distinct ductile failure characterized by large numbers of dimples. However, when, comparing the dimpling to that in the welded area, figure 10, it can be seen that the dimples of the unaffected zone are larger and shallower. This may be attributed to two reasons: fewer microvoids are forming during this process, and mircovoid coalescence happens at a faster rate relative to the welded material. When considering the first reason, the higher strength of the material makes nucleating a void much more difficult; however, when it is formed, it has the ability to grow at a faster rate. In addition, if the voids are growing faster relative to the fine grains, elongation will be lost and ductility will be reduced. This interpretation is in agreement with the data collected from table 3 which compares the values for failure strain. The microvoid coalescence from figure 11 also appears to be much more refined than the highly ductile failures seen in figure 10.

3.3 Strain Gradient Evolution During Loading

The microstructural distribution inside the friction stir weld has been widely documented. Within the weldment, there exists the weld nugget, TMAZ, and HAZ. These zones have quite pronounced effects on the mechanical properties. This is because they are formed as a result of dynamic recrystallization. Dynamic recrystallization is a process in which grains are strained in such a large amount that a lower energy state is achieved by recrystallization. This technique has been used widely to create very small grained material, which has high strengths due to the Hall-Petch relationship. This relationship holds true locally; however, another heat generated during FSW softens the grains. The heat allows for dislocation mobility coupled with annihilation due to non-conservative dislocation motion. The resulting structure follows Hall-Petch on the local scale, or the heat-affected zone; but outside this weld, it is significantly softer than the unaffected material.

Since the mechanical results are so closely related to the microstructural zones, a mismatch in material properties will exist. This will create a localized elevated stress level and non-uniform straining. This result is best seen in the areas around the weld in sections 2, 3, and 4. When comparing the strain gradient to that of the unaffected material in zones 12 and 13, a very unique behavior is observed. This behavior is termed strain-gradient hardening (*10)*. In strain-gradient hardening, adjacent zones with mismatching material properties results in higher work-hardening rates by the necessity to create geometrically necessary dislocations. It prevents the material from undergoing significant void formation or grain overlap.

The strain gradient evolution and hardening can be shown using the results of the digital image correlation. When comparing these results to the relative microstructural distribution, it is clear that there are very evident effects on the mechanical properties. In order to compare across specimens, the strain fields are considered during the elastic regime, at yielding and ultimate tensile strength, and just prior to failure. When examining these characteristics, a clear field is shown based on the microstructural properties.

From figure 14A, it is evident that the micrsostructure is homogeneous. Figure 14B shows the strain field during the elastic loading regime, which shows a generally constant strain field. In contrast, figure 14B shows the section at yielding. Of particular note, there appears to be the development of a strain-hardening regime. At the upper half the specimen, the strain field is significantly higher. This is due to the localized yielding. Additional strain fields are shown in the middle and bottom half; however, this is not uncommon in isotropic materials. This is due to the formation of geometric flaws forming along the tensile axis. This is evidenced by the local strain maximum along the tensile edges. As the material strains further, these areas work harden and the field is removed. As the material work hardens, the strain fields become less important, as shown in figure 14D, which shows the material at the ultimate tensile strength. At this point, the geometric instability has formed and the ability of the specimen to maintain the load is lost. Final failure is shown in figure 14E, just prior to failure. As seen in this picture, a neck has formed and is showing a local strain as high as 24%. This lack of clear strain gradient formation and evolution is characteristic of a material with the constant microstructure.

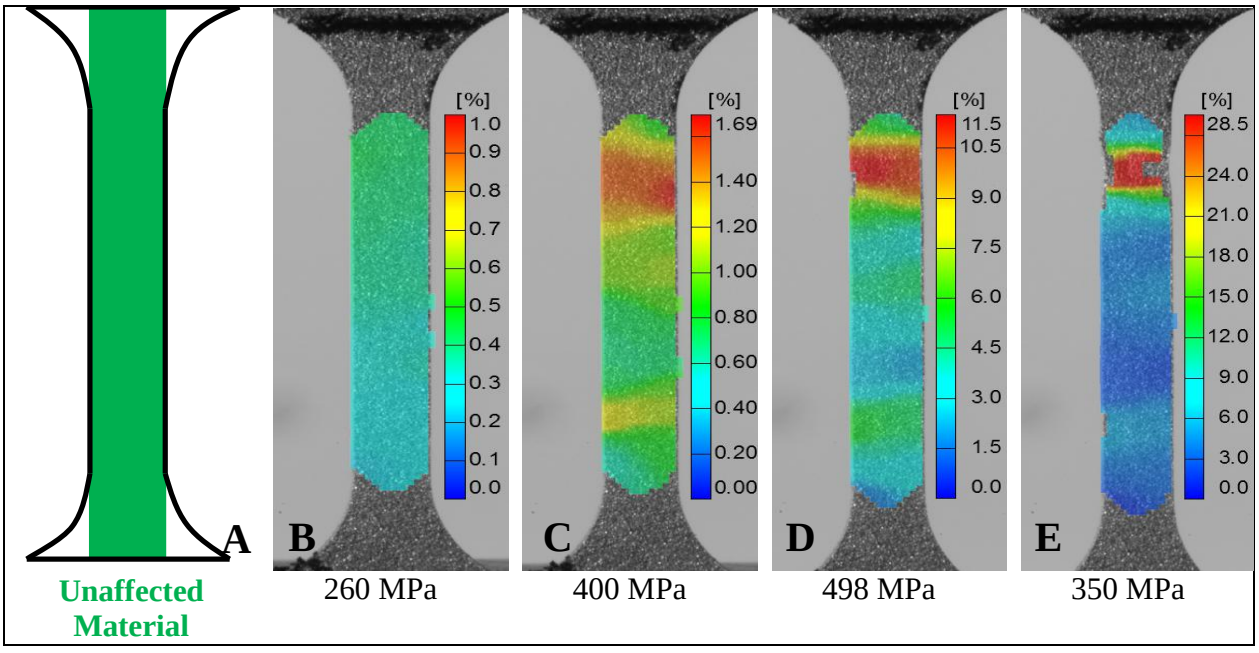

Figure 14. Strain-gradient evolution in the 11-X sample (unaffected zone).

In contrast to the unaffected zone, the section taken from inside the weld (section 2) displays very unique behavior due to its microstructure. As shown earlier, section 2 has mechanical properties vastly different than that of the unaffected material, specifically, a lower modulus of elasticity, yield point, UTS, and higher failure strain. This is due to the microstructural distribution inside of the tensile samples which include areas of the weld nugget, TMAZ and HAZ. These microstructures have a large effect on mechanical properties of the samples.

This evolution based on microstructure is much more apparent in figure 15, which shows the strain gradient evolution from elastic loading to onset of yielding, UTS, and final failure. Figure 15B shows similar behavior to that of the unaffected material, in particular, there is no clear strain gradient. However, a trend begins as shown in figure 15C, which shows the behavior post yield. The material begins to yield near the bottom of the grip; however, a clear strain gradient begins to form, in particular, a symmetric gradient about the center. This behavior is unique to this sample because it begins yield at the HAZ zone. Previous studies have shown that the HAZ zone has the lowest yield strength because it has the largest grains with relatively low dislocation densities. The weld nugget, a region shown to have very fine equiaxed grains due to the nature of the dynamic recrystallization process, is located in the center. On either side of it is the TMAZ, which has slightly lower yield strength due to the local Hall-Petch effect.

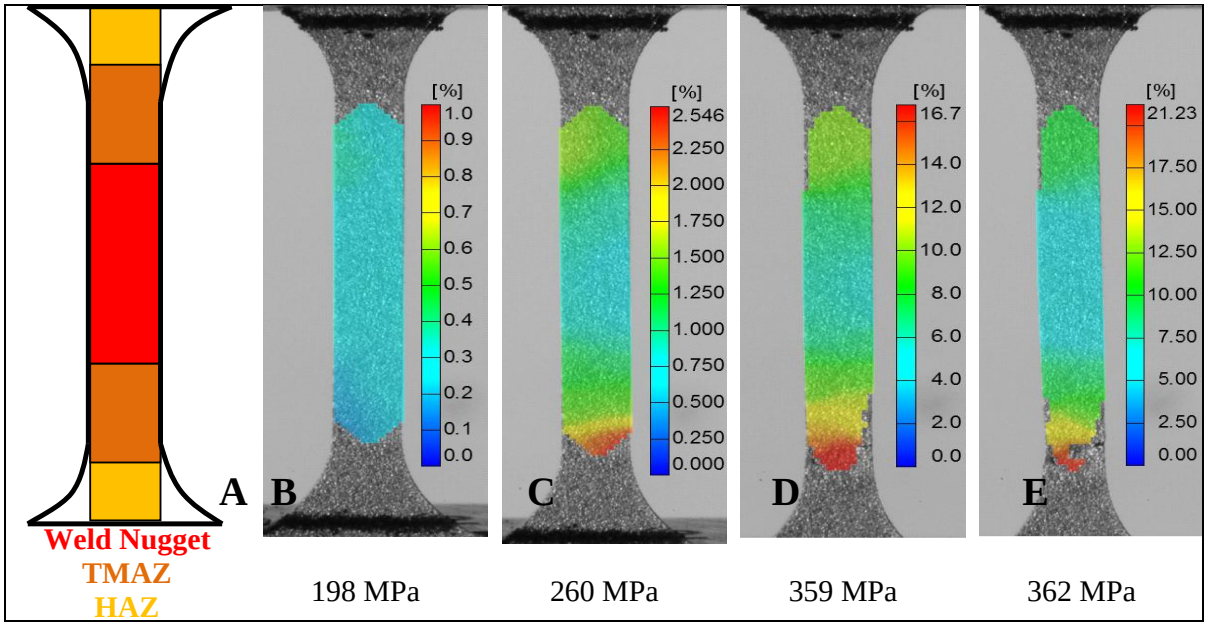

Figure 15. Strain-gradient evolution in the 2-X sample.

This trend continues to be seen in figure 15D, which shows the material at the ultimate tensile strength. At this time, the strain profile maintains a profile where the middle section has strained the least. This is because the hardest grains are located in the center. A geometric instability has begun to occur at the bottom, and final failure is shown in figure 15E. Of particular note, after failure, the final plastic strain accumulated can be documented. As shown in figure 15E, the

plastic strain also maintains the strain-field profile. This behavior is not seen in unaffected samples in which the effect of the strain field is minimized by local work hardening phenomenon.

When examining the through-thickness center weld sample, it is evident that the strain gradient hardening is occurring and is microstructurally related, as the microstructural zones are shown schematically in figure 16A. From this, it can be seen that two distinct microstructural zones have developed within the weld nugget itself. These zones form through the dissipation of the heat flux, as previous studies have shown, as much as 86% of the heat flux is generated from the shoulder (*12*). In the upper weld nugget, there are coarser grains which are the result of the grain growth after dynamic recrystallization. The finer grains are on the bottom half of the sample.

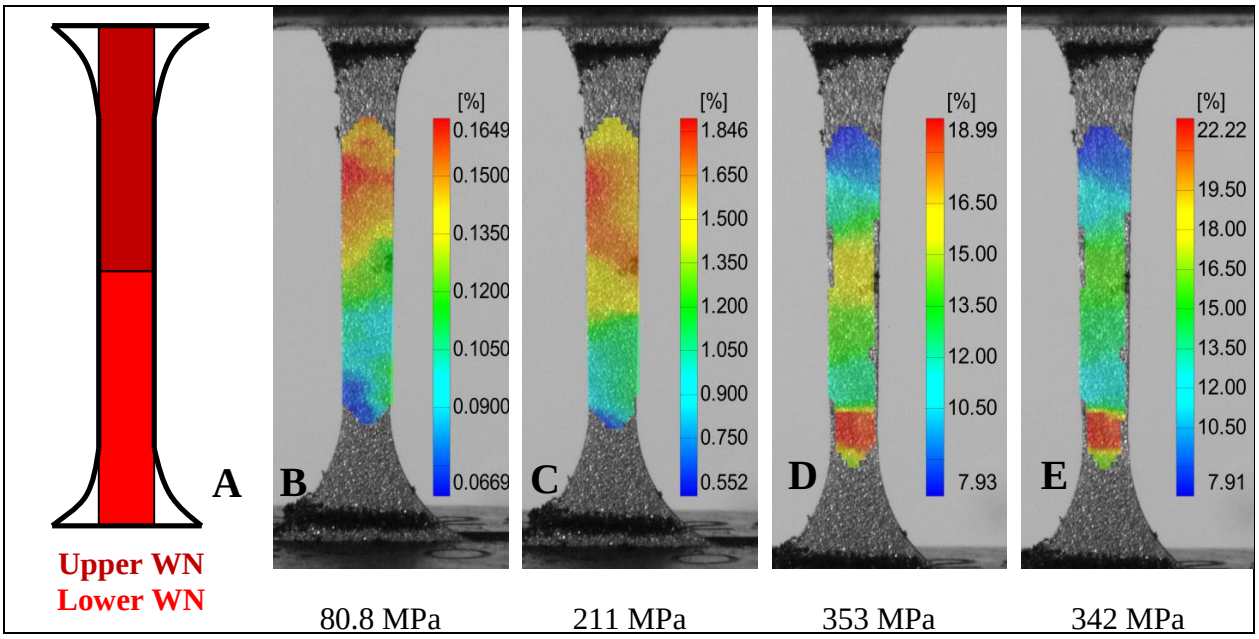

Figure 16. Strain-gradient evolution in the 2-Z direction sample.

From figure 16B, during the elastic loading from the macroscopic stress strain curve, there is a large region of strain occurring in the coarser grains on the top. This is indicative of a localized yielding, likely as a result of the grain structure and related to a localized relative Hall-Petch effect. Figure 16C, taken from the point of macroscopic yielding, shows evidence that the two structures are straining non-uniformly; specifically, the upper structure is showing higher total strain than that of the lower structure. The difference from the earlier picture is evident as the high stress concentration shown in the upper left of figure 16b has dissipated into the material as a function of work hardening.

The work-hardening effect is seen in near the UTS in figure 16D, which shows that the strain fields in the upper half are no longer higher than the rest of the sample. It has work hardened to a point where its response is similar to that of the lower weld nugget. Additionally, a large strain region exists in the center of the specimen. This is a result of the localized elevated stress level

that occurs due to the mismatch in material properties. The neck forms in the lower structure shown in figure 16e, while the structure at the top remains at a lower strain state. The neck forms in the lower weld nugget because of the lower saturation dislocation density that was discussed early. Finer grains have a lower saturation dislocation, i.e., the density at which the grain can no longer support additional dislocations. Failure is determined by which material's work hardenability saturates. In this case, the lower weld nugget has finer grains and will saturate faster than the coarser grains and, hence, failure will occur in the lower weld nugget.

4. Summary and Conclusions

4.1 Summary

Two plates of AA-2139 were joined using FSW, and tensile samples were extracted from various regions in the plate. It was determined that spatial considerations exist only in the area directly around the weld zone, which is a direct result of the development of the weld nugget, TMAZ, and HAZ. The weld nugget displayed unique properties that showed the existence of an upper and lower weld nugget, which was the result of heat dissipation through the material. The differences in microstructure lead to strain gradients within the material, which explains the unique mechanical behavior inside the weld zone; in particular, higher failure strains and lower UTS and yield strengths.

4.2 Future Work

Further characterization of the weld is necessary for implementation in finite-element (FE) models for blast loading. In particular, characterization of the upper weld nugget and lower weld nugget mechanical properties will be evaluated. Additional tensile samples will be cut in the weldment, with particular attention being paid to where the samples are being taken from with respect to the microstructural zones. Rate-dependent properties will be determined in both a uniaxial and multiaxial response using Split Hopkinson Tensile Bar and shock loading, respectively. These mechanical properties will be used as input to FE models to predict the failure of FSW joints.

5. References

1. Thomas, W. M.; Nicholas, E. D.; Needham, J. C.; Murch, M. G.; Temple-Smith, P.; Dawes, C. J. *Friction Stir Butt Welding*. U.S. Patent 5,460,317, 1995.

2. Midling, O. T. *Friction Stir Welding.* U.S. Patent 5,813,592, 1998.

3. Mahoney, M. W.; Rhodes, C. G.; Flintoff, J. G.; Spurling, R. A.; Bingel, W. H. Properties of Friction-Stir-Welded 7075 T651 Aluminum. *Metalurgical and Materials Transactions A* **1998**, *29*.

4. Hirata, T.; Oguri, T.; Hagino, H.; Tanaka, T. Influence of Friction Stir Welding Parameters on Grain Size and Formability in 5083 Aluminum. *Material Science and Engineering A* **2007**, *456*, 334–349.

5. Sutton, M. A.; Yang, B.; Reynolds, A. P.; Taylor, R. Microstructural Studies of Friction Stir Welds In 2024-T3 Aluminum. *Materials Science and Engineering A* **2002**, *323*, 160–166.

6. Sullivan, A.; Robson, J. D. Microstructural Properties of Friction Stir Welded and Post-Weld Heat-Treated 7449 Aluminium Alloy Thick Plate. *Materials Science and Engineering*: *A* **2008** *478*, 351–360.

7. International Alloy Designations and Chemical Composition Limits for Wrought Aluminum and Wrought Aluminum Alloys. *Registration Record Series - Teal Sheets.* The Aluminum Association: Arlington, VA, February 2009.

8. Yuana, H.; Wanga, Q. F.; Zhanga, J. W.; Liua, W. C.; Gaob, Y. K. Effect of Grain Shape on the Texture Evolution During Cold Rolling of Al–Mg Alloys; *Journal of Alloys and Compounds* **2011**, *508*, 922–928.

9. Suhuddin, U. F. H. R.; Mironov, S.; Sato, Y. S.; Kokawa, H. Grain Structure and Texture Evolution During Friction Stir Welding of Thin 6016 Aluminum Alloy Sheets. *Materials Science and Engineering A* **2010**, *527*, 1962–1969.

10. Courtney, T. H. *Mechanical Behavior of Materials*; 2nd ed.; The McGraw-Hill Corporation: Boston, MA, 2000.

11. Lee, W. *Dynamic Microstructural Characterization of High Strength Aluminum Alloys.* North Carolina State University: Raliegh, NC, 2008.

12. Schmidt, H.; Hattel, J.; Wert, J. An Analytical Model for the Heat Generation In Friction Stir Welding; *Modelling Simul. Mater. Sci. Eng.* **2004**, 143–157.

NO. OF COPIES	ORGANIZATION
1 (PDF only)	DEFENSE TECHNICAL INFORMATION CTR DTIC OCA 8725 JOHN J KINGMAN RD STE 0944 FORT BELVOIR VA 22060-6218
1	DIRECTOR US ARMY RESEARCH LAB IMNE ALC HRR 2800 POWDER MILL RD ADELPHI MD 20783-1197
1	DIRECTOR US ARMY RESEARCH LAB RDRL CIO LL 2800 POWDER MILL RD ADELPHI MD 20783-1197
1	DIRECTOR US ARMY RESEARCH LAB RDRL CIO LT 2800 POWDER MILL RD ADELPHI MD 20783-1197
1	DIRECTOR US ARMY RESEARCH LAB RDRL D 2800 POWDER MILL RD ADELPHI MD 20783-1197

NO. OF COPIES ORGANIZATION

2 DARPA
M MAHER
J GOLDWASSER
3701 N FAIRFAX DR
ARLINGTON VA 22217-5600

2 DIRECTED TECHNOLOGIES INC
J PEREZ
R SANDS
3601 WILSON BLVD
STE 650
ARLINGTON VA 22201

1 US ARMY TARDEC
AMSRD TARR
D TEMPLETON MS263
6501 E 11 MILE RD WARREN
MI 48397-5000

1 B JUSTUSSON
15956 CRYSTAL DOWNS EAST
NORTHVILLE MI 48168

1 J MEDINTZ
6650 PRUE RD
APT 1026
SAN ANTONIO TX 78240

ABERDEEN PROVING GROUND

24 DIR USARL
RDRL SL
R COATES
RDRL WM
S KARNA
J MCCAULEY
RDRL WMM
J BEATTY
R DOWDING
P SMITH
J ZABINSKI
RDRL WMM A
J SANDS
D O'BRIEN
D SPAGNUOLO
RDRL WMM B
B CHEESEMAN
C FOUNTZOULAS
T SANO
M VANLANDINGHAM
C YEN
J YU

NO. OF COPIES ORGANIZATION

RDRL WMM D
R BRENNAN
W GREEN
RDRL WMM E
M BRATCHER
P DEHMER
G GILDE
J LASALVIA
P PATEL
RDRL WMM F
K DOHERTY

INTENTIONALLY LEFT BLANK.